Tensor Interpolation in Virtual Manufacturing Chains for Fiber Reinforced Composites

Constantin Krauß[1,*], Luise Kärger[1]

Karlsruhe Institute of Technology, Institute for Vehicle System Technology — Lightweight Technology, 2 Rintheimer Querallee, 76131 Karlsruhe, Germany

Abstract

Preeminent weight-specific mechanical properties predestine fiber-reinforced plastics for application in structural components. Virtual manufacturing chains (CAE-chains) capture a multi-step process sequence by interlinking models with corresponding constitutive laws for each process step. In common numerical solving techniques, spatial discretization of governing equations yields discrete solutions. Since mesh type and fineness are usually problem-specific, mesh-to-mesh mapping must be embedded in the data interfaces between the individual simulation steps. To receive meaningful data, the underlying averaging and interpolation schemes between non-congruent meshes must be mathematically and physically consistent. In engineering applications, interpolation of tensors is usually carried out component-based, treating each component as an independent scalar-field and thus neglecting the tensorial character. The work at hand gives an overview of sophisticated techniques that preserve specific tensor characteristics in interpolation. Compared to available approaches, an enhanced decomposition-based interpolation method is proposed, allowing for a generalization with more than two basic values. In the context of process simulation for short fiber-reinforced injection molding, the influence of the interpolation techniques is evaluated in a three-stage approach with increasing proximity to application. Firstly, mathematical examples demonstrate that component-based

*Corresponding author
Email address: constantin.krauss@kit.edu (Constantin Krauß)

interpolation can result in erroneous, non-monotonous tensor characteristics. Secondly, an analytically resolvable problem is derived, and the solution is compared to reconstructed tensors from different interpolation schemes. Thirdly, a numerical CFD-simulation is conducted. Field recovery via interpolation is performed and systematical errors are statistically evaluated. The results reveal significant biases for certain tensor characteristics induced by conventional component-wise interpolation. Overall, a reduction in systematic interpolation errors is achieved by the proposed decomposition-based interpolation.

Keywords: Virtual Manufacturing, Process Simulation, Injection Molding, Data Interfaces

1. Notation

Symbolic tensor notation is preferred throughout this work. Direction independent scalars are denoted by standard Latin and Greek letters, e.g. a, λ, F. First order tensors are represented by bold lower case letters, e.g. $\boldsymbol{p}, \boldsymbol{\gamma}$, whereas upper case Greek or Latin letters are used for 2^{nd}-order tensors such as $\boldsymbol{A}, \boldsymbol{E}$. Fourth order tensors are denoted by $\mathbb{C}, \mathbb{S}$. The linear mapping of an arbitrary lower order tensor by a corresponding higher order tensor, e.g. $\mathbb{C}\boldsymbol{E}$ as well as the composition of second and higher order tensors, e.g. $\boldsymbol{AB}$ are denoted without taking use of a particular operator symbol. Scalar products between two tensors of the same order are marked by a dot, e.g. $\boldsymbol{A} \cdot \boldsymbol{C}$. The dyadic outer product yields a tensor of order $m + n$ from the multiplication of a m by a n-order tensor, e.g. $\boldsymbol{a} \otimes \boldsymbol{A}$. The Frobenius Norm $\sqrt{\boldsymbol{A} \cdot \boldsymbol{A}}$ is used and abbreviated through $\|\boldsymbol{A}\|$. The rotation of an arbitrary order tensor is denoted by the Rayleigh Product $\boldsymbol{Q} \star \mathbb{S}$, where the 2^{nd}-order tensor $\boldsymbol{Q}$ is member of the special orthogonal group $SO(3)$. Arbitrary sized numerical arrays (e.g. components in a specific coordinate system) are denoted by indices, e.g. a_i, A_{ij} where the number of indices directly corresponds to their dimensionality. Two types of indices must be distinguished: iterators in a set of discrete values are denoted by upper case letters $I, J, \dots \in \mathbb{N}$, spatial components in the three-dimensional

space are denoted by lower case letters $i, j, \cdots = 1..3$. Unless otherwise indicated, Einstein's convention for summation holds, thus indices appearing twice in a single expression implying summation. Four-dimensional quaternions are denoted by an arrow-head above the Latin letter, such as in $\vec{q}$. For derivatives with respect to tensor fields $\boldsymbol{\phi}$ of arbitrary order, right-hand operators are used, such that $\operatorname{grad}(\boldsymbol{\phi}) = \lim_{\Omega\to 0} \Omega^{-1} \int_\Gamma \boldsymbol{\phi} \otimes \mathrm{d}\boldsymbol{s}$ and $\operatorname{curl}(\boldsymbol{\phi}) = \lim_{\Omega\to 0} \Omega^{-1} \int_\Gamma \boldsymbol{\phi} \times \mathrm{d}\boldsymbol{s}$ respectively, where Ω is the integration domain, closed by its boundary Γ with outward normal $\boldsymbol{s}$.

2. Introduction

Fiber-reinforced plastics (FPRs) possess exceptional weight-specific mechanical properties. Hence, this class of materials has shown increased market share especially in weight-sensitive industrial sectors, e.g. automotive or aviation. In contrast to most other engineering materials, both the macroscopic-homogeneous composite material and the actual load-bearing component are usually produced in-situ. The well-known Resin Transfer Molding (RTM) process and other liquid composite molding processes can serve as examples, where fiber and matrix merging and bonding take place in the molding tool [1]. In alternative manufacturing processes fiber and matrix are usually matched in upstream processes (prepreg technology) or immediately prior to component production (direct processes) [2]. As a consequence, the characteristics of the final composite material are mainly determined during the course of the manufacturing process. Several investigations have shown pronounced influence of the manufacturing parameters on the final load-bearing capacity [3, 4, 5]. This holds especially for high-performance components that take maximum advantage of the anisotropic characteristics of FRPs [3, 6]. Hence, holistic composite design requires taking the material's entire prehistory along the process route into account. Since physics and general material behavior usually change over the course of the process, different types of simulations have to be conducted and linked in so-called CAE-chains in order to capture the relevant physical and

chemical mechanisms in digital twins for process and part [3, 6, 7].

Simulation of manufacturing processes, structural simulation of load-bearing components and homogenization methods in multi-scale approaches of FRPs require the use of tensors in order to describe higher-dimensional and direction dependent (non-)linear interrelations on kinematic, kinetic and constitutive level. Although governing equations of the underlying physical problems are usually formulated by the means of classical continuum mechanics, common solution approaches take use of numerical methods such as Finite Element Method (FEM), Finite Difference Method (FDM) or Finite Volume Method (FVM) operating on discretized domains. Instead of (continuous) fields, that assign values to each material point $\boldsymbol{X}$ (Lagrangian approach $\phi_{\text{Lagrange}} : \mathbb{R}_+ \times (\boldsymbol{X} \in \Omega) \mapsto \mathbb{R}^n$) or each spatial point $\boldsymbol{x}$ (Eulerian approach $\phi_{\text{Euler}} : \mathbb{R}_+ \times (\boldsymbol{x} \in \Omega) \mapsto \mathbb{R}^n$)[1] in the solution domain Ω at an given point in time $t \geq t_0 \geq 0$, only a finite number of values is assigned respectively computed for each field.

When transferring discrete field data from one simulation module to another involves changing mesh types or mesh topologies, an intermediate data-mapping step becomes mandatory [7]. To minimize information loss as result of this mapping operation, the underlying averaging and interpolation methods have to be optimal from an informatics-algorithmic perspective, but are also required to fulfill field-specific boundary conditions to be mathematically and physically consistent.

Scope of This Work. The work at hand focuses on interpolation techniques for 2^{nd}-order symmetric tensor fields like fiber orientation or stress tensors. It may be noted, that the numerical investigations are carried out in a composite context, but do not restrict to this specific domain. The overall aim is to integrate such techniques into virtual manufacturing workflows for composites and thus minimize systematical errors when transferring tensorial field data between deviating discretizations.

[1] a bijective relation usually exists except for singular boundaries

This paper is structured as follows: Section 3 provides an overview of the underlying mathematics, containing theory on the basic interpolation concepts and their advantageous and adverse properties in terms of physical interpretation and numerical feasibility. In addition, generalization of approaches are proposed that allow for more than two basic values as input and therefore enable application in two- and three-dimensional problems. In Section 4 an example problem of practical significance and its analytical solution are introduced. Selected interpolation methods are tested upon this example and their performances are compared on various error metrics. Finally, a numerical process simulation example is provided. Interpolation techniques are applied to perform local field recovery. The induced errors are statistically evaluated for different densities of information.

3. Interpolation Methods for 2$^{\text{nd}}$-Order Symmetric Tensor Fields

The section starts with the relevant theoretical background of tensor algebra, distance measurements between tensors and associated metrics. Subsequently, a categorization proposal of interpolation schemes is introduced. Finally, occurring differences in the regarded interpolation schemes are discussed and visualized by means of purely mathematical example problems.

3.1. The Set of Symmetric Tensors

The set of symmetric tensors $Sym : \{\boldsymbol{A} \in \text{Lin} : \boldsymbol{x} \cdot \boldsymbol{A}\boldsymbol{y} = \boldsymbol{y} \cdot \boldsymbol{A}\boldsymbol{x} \forall \boldsymbol{x}, \boldsymbol{y} \in \mathcal{V} \backslash \{\boldsymbol{0}\}\}$ can be interpreted as entirety of all tensors $\boldsymbol{A}$ that are identical to their transposes $\boldsymbol{A}^{\top}$. As an ultimate consequence of this definition, the Eigenvalues of this group of tensors are real-valued in each case [8]. Therefore, a large proportion of tensors describing physical quantities – or at least their observable part – have to be symmetric. Additionally, symmetric tensors allow for the determination of at least one corresponding real-valued ortho-normal system of distinct Eigenvectors. The set of symmetric tensors can be further subdivided by means of the signs of the occurring Eigenvalues. For visualization purposes

of 2^{nd}-order symmetric tensors in a fixed coordinate frame, superquadric glyph rendering, as proposed in [9] and generalized in [10], will be used in sections 3, 4 and 5.

3.2. Interpolation Techniques and Requirements for Tensor Fields

Formally, an interpolation scheme $\bar{\phi} = f(\phi_I, w_I)$ is defined as a mapping f taking a set of $N \geq 1$ discrete values ϕ_I and their corresponding weights $w_I \in [0; 1]$ as arguments. The normalized weights have to satisfy the completeness condition $\sum_I^N w_I = 1$ [11]. In spatial interpolation, weights are usually determined as function of the relative distance between interpolation location and basis point location(s). Various explicit approaches, e.g. the nearest point method, polynomial shape functions on (un)structured grids or Shepard's inverse distance formulation [12] are well-known and integrated into commercial and open-source codes. With increasing computational power, more advanced implicit approaches, such as the radial basis function interpolation (RBF) [13] and its derivatives become feasible [14]. Herein, the weights are computed as approximate solution to an optimization problem on function spaces.

In this work, the expansion of interpolation techniques, which were originally formulated for scalar input, towards the set of 2^{nd}-order symmetric tensors will be investigated with particular emphasis set on the involved averaging schemes. Thus, weights are not subject of investigation and assumed to be given in the present section.

The boundary condition $w_J = 1$ and $w_I = 0$, $I \neq J \rightarrow \bar{\boldsymbol{\phi}} = \boldsymbol{\phi}_J$ stated for scalar interpolation, can be adapted to tensorial input without further modification. For tensor fields, however, results must not additionally depend on the chosen basis [15]. Hence, the mapping $\boldsymbol{f}$ has to be invariant under any rotation and satisfy the isotropy condition

$$\boldsymbol{Q} \star \bar{\boldsymbol{\phi}} = \boldsymbol{f}\left(\boldsymbol{Q} \star \boldsymbol{\phi}_I, w_I\right), \quad \forall\, \boldsymbol{Q} \in SO(3). \tag{1}$$

In principle, two groups of interpolation techniques are to be distinguished: *Global methods* operate directly on the input tensors, whereas in *decomposition-*

based methods specific characteristics are interpolated separately and the interpolant is constructed by means of re-assembly.

In the following, a selection of different available tensor interpolation methods will first be presented and subsequently evaluated comparatively with regard to different criteria afterwards.

3.3. Global Interpolation Methods

Global interpolation techniques operate directly on the input tensor-valued arguments. The resulting weighted averages are usually a solution to an optimization problem of the type:

$$\bar{\boldsymbol{A}} = \arg\min_{\boldsymbol{A}} \sum_{I}^{N} w_I d^2 \left(\boldsymbol{A}_I, \boldsymbol{A}\right), \tag{2}$$

where d is a distance measure that is connected to a specific metric. The value obtained in this way is referred to as weighted Frechet mean [16]. Depending on the structure of d, there may exist closed-form explicit solutions or implicit solutions, which must be solved using numerical approaches.

3.3.1. Euclidean Interpolation (EU)

The simplest interpolation of a continuous scalar valued function $\bar{\phi}$ can be interpreted as weighted arithmetic average of $N \in \mathbb{N}$ function values ϕ_I. The averaged value is computed in accordance to $\bar{\phi}_{\mathrm{EU}} = \sum_I^N w_I \phi_I$. This method owes its name to the fact that the interpolated value is located on the hyperplane within the N-dimensional Euclidean-space spanned by the weights w_I and is also referred to as linear interpolation (LERP) [17]. With respect to tensors, this approach is extended to components in a common ortho-normal basis yielding

$$\bar{A}_{\mathrm{EU},ij} = \sum_{I}^{N} w_I A_{I,ij} \tag{3}$$

by formula. This is the explicit solution of the corresponding optimization problem, where the Euclidean distance $d = \|\boldsymbol{A}_I - \boldsymbol{A}_J\|$ is used to minimize the cumulative distances between basis values and their weighted average using the Frobenius norm as distance measure. The Euclidean approach treats

each component as independent scalar field. The comparatively simple explicit expression stated in Eqn. (3) works for an arbitrary number of input arguments and underlines the numerical superiority of this approach, especially for the case that all discrete tensor values are stored with respect to an explicit common basis and no upstream coordinate transformation is required.

3.3.2. Riemannian Interpolation (RIE)

The set of symmetric positive (semi-)definite tensors can be interpreted as smooth and curved Riemannian manifold [18, 19, 20]. Due to this curvature the usage of the Frobenius norm, which assumes flat Euclidean space as distance measure is not valid. Instead, the associated logarithmic map is used and yields

$$d_{\mathrm{RIE}}\left(\boldsymbol{A}_1, \boldsymbol{A}_2\right) = \left|\left|\ln\left(\boldsymbol{A}_1^{-\frac{1}{2}} \boldsymbol{A}_2 \boldsymbol{A}_1^{-\frac{1}{2}}\right)\right|\right| \tag{4}$$

as the natural distance between two tensors $\boldsymbol{A}_1, \boldsymbol{A}_2$ [21]. From inserting this distance formulation in Eqn. (2), the solution follows as:

$$\bar{\boldsymbol{A}}_{\mathrm{Rie}} = \boldsymbol{A}_1^{\frac{1}{2}} \exp\left(w_2 \ln\left(\boldsymbol{A}_1^{-\frac{1}{2}} \boldsymbol{A}_2 \boldsymbol{A}_1^{-\frac{1}{2}}\right) \boldsymbol{A}_1^{\frac{1}{2}}\right), \quad N = 2 \tag{5}$$

$$\sum_{I}^{N} w_I \bar{\boldsymbol{A}}_{\mathrm{Rie}}^{-\frac{1}{2}} \boldsymbol{A}_I \bar{\boldsymbol{A}}_{\mathrm{Rie}}^{-\frac{1}{2}} = 0, \quad N > 2. \tag{6}$$

Hereby, a case distinction becomes necessary: if only two input arguments are provided, an explicit expression exists and can be computed straightforwardly. If the number of basis values exceeds 2 however, only an implicit solution can be derived [22]. Computation is performed by taking use of an iterative method.

3.3.3. Log-Euclidean (LOG)

Since the implicit characteristic of the affine Riemannian approach, requires several computational expensive evaluations of non-linear tensor functions, this method is not feasible for complex problems. Against this backdrop, a novel approach has been introduced in [23]: the Log-Euclidean tensor interpolation technique is basically a generalization of the geometric mean for scalars towards

symmetric positive definite (SPD) tensors [24]. Thus the explicit follows as

$$\bar{\boldsymbol{A}}_{\mathrm{LOG}} = \sum_{I}^{N} \exp\left(w_I \ln\left(\boldsymbol{A}_I\right)\right). \tag{7}$$

The associated distance is defined as

$$d_{\mathrm{LOG}}\left(\boldsymbol{A}_1, \boldsymbol{A}_2\right) = \mathrm{tr}^{\frac{1}{2}}\left(\left(\ln\left(\boldsymbol{A}_1\right) - \ln\left(\boldsymbol{A}_2\right)\right)^2\right). \tag{8}$$

Hence, a straightforward computation is feasible, regardless of the number of input basis arguments. Besides the application in interpolation problems, the Log-Euclidean approach has recently gained relevance in fluid and solid mechanics' context. Hameduddin and Zaki [25] apply the approach in order to improve the accuracy of visco-elastic turbulence models. Gao et al. [26] and Huang et al. [27] use the technique for the determination of mean stress measurements. Brethes et al. [28] and Shakkor and Park [29] have embedded the algorithm in their implementation of PDE solving applications.

It may be noted, that the above appearing powers, logarithms and exponentials formulas are the associated isotropic tensor functions and must not be confused with the scalar mappings [30]. The application of negative exponents and tensor logarithms in the context of the Riemannian and the Log-Euclidean approaches are unambiguous for strictly positive definite tensors only, therefore restricting those techniques to this specific subset [31].

3.4. Decomposition-Based Interpolation Methods

In several scenarios, the specific invariants of the regarded tensors are of particular relevance. On this account, numerous efforts have been conducted in recent years in order to design interpolation techniques that put special emphasis on this characteristics. Driven by the increasing acceptance of medical diffusion tensor magnetic resonance imaging (DT-MRI), most of the progress has been achieved in the context of this field. Decomposition-based interpolation methods pursue the concept of interpolating invariants and orientation of tensors separately and independently. Afterwards, a reassembly step occurs yielding the interpolated result.

3.4.1. Eigendecomposition and Projector representation

The well-known Eigenvalue problem $\boldsymbol{A}\boldsymbol{p}_i = \lambda_i \boldsymbol{p}_i$ can be rewritten as spectral decomposition $\boldsymbol{A} = \boldsymbol{E}\boldsymbol{\Lambda}\boldsymbol{E}^{-1}$ using a tensor $\boldsymbol{E}$ constructed by the Eigenvectors $\boldsymbol{p}_i$ as column vectors. The tensor $\boldsymbol{\Lambda}$ contains the Eigenvalues. Its non-zero entries are located exclusively on the principal diagonal. Since the Eigenvectors are arbitrary in magnitude and also bidirectional, an infinite number of $\boldsymbol{E}$ tensors exists. If the Eigenvectors are normalized, $\boldsymbol{E}$ becomes an orthogonal tensor. By way of distinction, the symbol $\boldsymbol{R}$ is used for such normalized Eigenvector tensors. Due to its orthogonality, the inverse of $\boldsymbol{R}$ is identical to its transpose $\boldsymbol{R}^\top = \boldsymbol{R}^{-1}$. In this special case the spectral decomposition further simplifies to

$$\boldsymbol{A} = \boldsymbol{R}\boldsymbol{\Lambda}\boldsymbol{R}^\top \tag{9}$$

Herein, $\boldsymbol{R}$ may be interpreted as a pure rotational mapping from Eigensystem to a global basis. Despite the Eigendecomposition itself is unique, the tensor $\boldsymbol{R}$ is not [32]. Depending on the cardinality γ of different-valued Eigenvalues, four (for $\gamma = 3$), an infinite subset of SO(3) ($\gamma = 2$) or even $\boldsymbol{R} \in \mathrm{SO}(3)$ ($\gamma = 1$) fulfill equation 9 (cf. Figure 1).

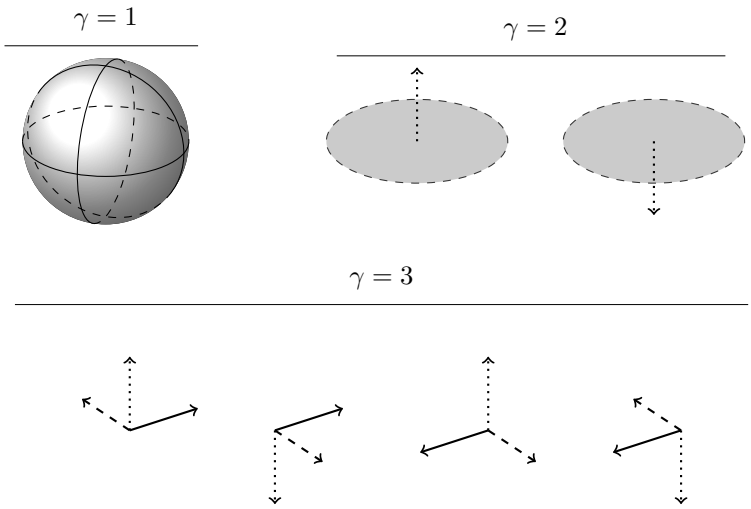

Figure 1: Arbitrariness of Right-Hand Eigensystems for different cardinalities γ. The linestyle of each axis gives the information about the corresponding Eigenvalue. For $\gamma = 1$ each Right-Hand system is an Eigensystem, for $\lambda = 2$ each pair of ortho-normal axes in the gray-colored planes form an Eigensystem with the dotted principal axis. For $\lambda = 3$ four different Eigensystems exist.

Another representation of $\boldsymbol{A}$ in terms of Eigenvalues and Eigenvectors can be achieved by

$$\boldsymbol{A} = \sum_{i}^{\gamma} \lambda_i \boldsymbol{P}_i. \tag{10}$$

This additive decomposition is referred to as projector representation of $\boldsymbol{A}$, since the 2^{nd}-order tensor

$$\boldsymbol{P}_i = \sum_{\alpha}^{\gamma(\lambda_i)} \boldsymbol{p}_\alpha \otimes \boldsymbol{p}_\alpha \tag{11}$$

is the projector corresponding to the i-th Eigenvalue λ_i with multiplicity $\gamma(\lambda_i) \in [1;3]$. Each set of projector tensors is unique for a given tensor $\boldsymbol{A}$ and suffices completeness $\sum_\alpha \boldsymbol{P}_\alpha = \boldsymbol{1}$, biorthogonality $\boldsymbol{P}_\alpha \cdot \boldsymbol{P}_\beta = 0 \quad \forall \alpha \neq \beta$ and idempotence $\boldsymbol{P}_\alpha^n = \boldsymbol{P}_\alpha \, \forall n \in \mathbb{R}$ [33].

3.4.2. Shape Interpolation

The shape of a 2$^{\text{nd}}$-order symmetric tensor can be expressed by a set of three linear-independent invariants. The most obvious example for such a set are the Eigenvalues γ_i. Actually, there are approaches from the area of image processing, that operate directly on the Eigenvalues, e.g. [34, 35]. However, [36] has shaped the concept of *orthogonal invariants* I_i and showed that those are well suited for physical problems. The derivatives of those invariants with respect to the tensor itself form a orthogonal basis, such that

$$\frac{\partial I_i}{\partial \boldsymbol{A}} \cdot \frac{\partial I_j}{\partial \boldsymbol{A}} = 0 \quad i \neq j. \tag{12}$$

In the context of [36], two sets of this kind have been proposed and labeled as K- and R- invariant. The K invariants consist of tensor trace K_1, the norm of the deviatoric, directional share K_2 and tensor mode K_3, while the R invariants are composed of tensor norm R_1, fractional anisotropy R_2 and also tensor mode $R_3 = K_3$.

$$K_1 = \operatorname{tr}(\boldsymbol{A}), \qquad K_2 = \|\boldsymbol{A}'\|, \quad K_3 = 3\sqrt{6}\frac{\det(\boldsymbol{A}')}{\|\boldsymbol{A}'\|^3} \tag{13}$$

$$R_1 = \|\boldsymbol{A}\|, \qquad R_2 = \sqrt{\frac{2}{3}}\frac{\|\boldsymbol{A}'\|}{\|\boldsymbol{A}\|}, \quad R_3 = K_3. \tag{14}$$

Herein, $\boldsymbol{A}' = \boldsymbol{A} - \operatorname{tr}(\boldsymbol{A})/3$ denotes the deviatoric part of the tensor. Via a geometric access, the K invariants can be interpreted as cylindrical coordinates in the Eigenspace of $\boldsymbol{A}$ spanned by its projectors $\boldsymbol{P}_i$ with axial height K_1, radial distance K_2 and azimuthal angle K_3, while R invariants correspond to spherical coordinates composed by radius R_1, inclination R_2 and again azimuthal angle R_3. In both cases, the zenith direction is co-linear with the isotropic line obeying $\lambda_1 = \lambda_2 = \lambda_3$. Fig 2 is supposed to illustrate the correlations mentioned above and displays the generalized gradient of both invariant sets.

Since the orthogonal invariant sets are constructed to be independent of one another, scalar interpolation techniques become feasible. Numerous investigations and applications can be found in literature, e.g [37, 38, 39, 40, 41]. All works have used linear interpolation on the according set of orthogonal invari-

ants

$$\bar{K}_i = \sum_I^N w_I K_{Ii} \qquad \text{or} \qquad \bar{R}_i = \sum_I^N w_I R_{Ii} \tag{15}$$

[37] have proposed methods to compute the interpolated shape tensor $\bar{\mathbf{\Lambda}}$ respectively the interpolated set of Eigenvalues from the K or R invariants. It is stated within this work that this back calculation is restricted to positive semidefinite tensors. However, with no loss of generality the K invariants can be analytically reconstructed to unique Eigenvalues even if the tensor in question is negative (semi)definite or indefinite.

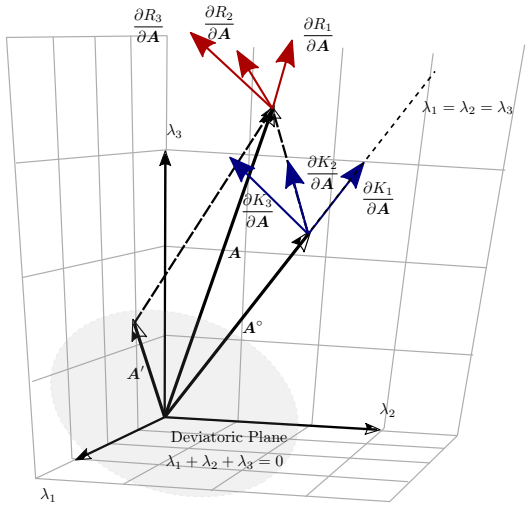

Figure 2: Graphical interpretation of the R- and K-sets of invariants and their derivatives with respect to $\boldsymbol{A}$ in the Eigenspace of $\boldsymbol{A}$.

3.4.3. Orientation Interpolation

The orientation of a tensor is fully characterized by the orthogonal tensor $\boldsymbol{R}$ in eqn. 9, which can be understood as mapping related to a rigid body rotation. The theory of rotations is comprehensively investigated due to countless applications in computer graphics and inverse kinematics. Therefore, a broad variety of more or less sophisticated interpolation approaches exists for

this classes [42, 43, 44, 45], that can and have been adopted for orientation interpolation purposes.

Unit Quaternion Interpolation. Operating directly on rotation matrices is uncommon in modern codes due to two practical reasons: First, storing and accessing all nine components is unfavorable from a numerical point of view, since the set of rotations $SO(3)$ is a three parameter group. Second, the set $SO(3)$ is not closed under addition, and standard algebraic operations may yield non-orthogonal tensors. This is especially true when linear interpolation is applied to two or more orientation tensors. Most work in literature, that used a decomposition approach has applied this method for orientation interpolation nonetheless taking the inevitably induced error into acceptance. Instead, rotation related operations are conducted by means of unit quaternions $\vec{q} \in SU(2)$, with $\|\vec{q}\| = 1$. Here, $SU(2)$ is the special unitary group that is connected via a homorphism to $SO(3)$. Therefore, unit quaternions can be interpreted as three-dimensional rotations. Thus, the inverse operation $\vec{q}^{-1}$ simplifies to changing the sign of the imaginary part of the quaternion such that $\vec{q}\,\vec{q}^{-1} = 1$.

For tensor interpolation purposes, Gahm and Ennis [46] firstly applied quaternion based orientation interpolation. However, they remain with an academic example considering only two basis values: the unique case, in which an explicit solution exists [47]. To the knowledge of the authors, there is no work published that proposes or applies a generalized approach in the context of tensor interpolation. Therefore, this gap should be closed with the following approach. A related Frechet mean $\bar{\vec{q}}$ of $N \in \mathbb{N}$ unit quaternions $\vec{q}_I$ can be computed with fast convergence in a simple predictor-corrector approach, as analytical expressions for logarithmic and exponential maps exist for $SU(2)$. Those preserve distance and angle when mapping onto respectively from the tangent hyperplane. The algorithm, outlined in proc. 3.4.3 using pseudo-code, specifies the command sequence. Additionally, figure 3.4.3 illustrates the fundamental procedure on the unit circle S_1, since the actual four-dimensional problem is not accessible through human spatial perception. The conducted steps, principles and terms

remain the same, though.

Algorithm 1 Determination of the Frechet mean $\bar{\vec{q}}$ in pseudo code

procedure QUATERNION INTERPOLATION($\vec{q}_I$, w_I, ε)

  $\bar{\vec{q}} \leftarrow \sum_I w_I \vec{q}_I$ ▷ Guess $\bar{\vec{q}}$ using Euclidean metric

  $\bar{\vec{q}} \leftarrow \bar{\vec{q}}/\|\bar{\vec{q}}\|$ ▷ Map $\bar{\vec{q}}$ onto S^3

  while $\|\vec{\delta}\| \geq \varepsilon$ **do** ▷ Repeat until convergence

    $\underline{\vec{\mathrm{lm}}}_{\bar{q}} \leftarrow \ln\left(\left(\bar{\vec{q}}\right)^{-1} \vec{q}_I\right)$ ▷ Map $\vec{q}_i$ to the tangent hyperplane

    $\vec{\delta} = \sum_I w_I \vec{\mathrm{lm}}_{\bar{q},I}$ ▷ Euclidean average on hyperplane

    $\bar{\vec{q}} \leftarrow \bar{\vec{q}} \exp\left(\vec{\delta}\right)$ ▷ Update $\bar{\vec{q}}$

  return $\bar{\vec{q}}$

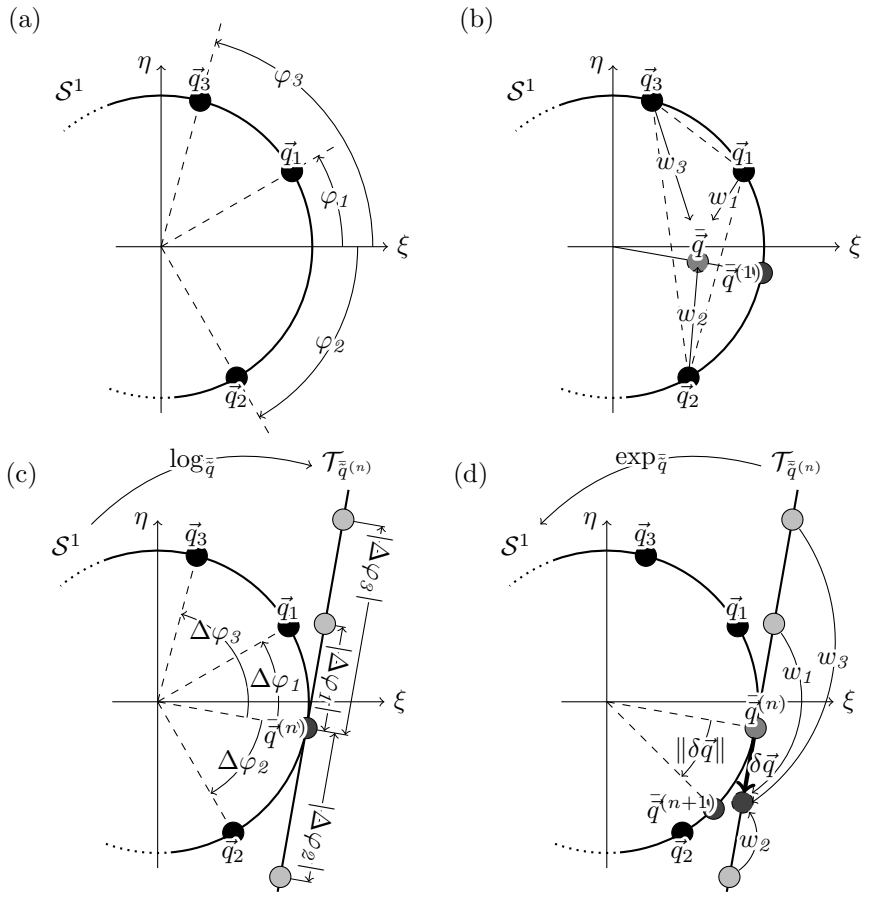

Figure 3: Determination of Frechet mean on S_1 for three basis values $\vec{q}_I$(a). An initial guess for $\bar{\vec{q}}$ is made upon linear interpolation and downstream normalization yielding $\bar{\vec{q}}^{(0)}$ (b). A tangent line $\mathcal{T}$ is spanned at the location of the initial guess and basis values are transferred to the tangent line using the logarithmic map (c). In the predictor, step Euclidean averaging is conducted on the flat tangent line. A residual $\delta\vec{q}$ to the initial guess is found and mapped back onto the manifold using the exponential map. Thereby, the interpolated value $\bar{\vec{q}}$ is updated. Step (c) and (d) are repeated until the desired convergence is reached.

The iterative algorithm shows fist-order convergence behavior. For 1000 randomly created samples error fell below floating point accuracy within the first 8 iterations. Convergence behavior can be improved by using a gradient-based approach. However, evaluating complex derivatives, as outlined by Kim et al. [48], might lead to an increase in overall runtime.

Dyadic Interpolation. The aforementioned sign ambiguity of the normalized Eigenvectors results in at least four equivalent candidates for orientation tensors $\boldsymbol{R}_I$. While approaches exist to select a favorable combination based on geometric argumentation, this problem is of factorial time complexity with respect to the number of input basis values. In order to circumvent this problem, the so called *dyadic tensor-based interpolation* is introduced in [46]. This method takes use of the fact that the projector decomposition (10) is based upon the bi-linear dyadic product of the Eigenvectors. Thus, permuting the sign of $\boldsymbol{p}_i$ leaves the corresponding projector $\boldsymbol{P}_i$ unaffected [49].

In this approach an approximation $\boldsymbol{M}$ for the orientation tensor is computed and weighted with the interpolated Eigenvalues stored in $\boldsymbol{\Lambda}$. Finally, the interpolated orientation tensor $\boldsymbol{R}$ is computed using a polar decomposition and dropping the stretch part $\boldsymbol{U} \in SYM$.

$$\bar{\boldsymbol{\Lambda}}\bar{\boldsymbol{M}} = \bar{\boldsymbol{R}}\boldsymbol{U} \tag{16}$$

The reader is referred to [46] for a detailed derivation of obtaining $\boldsymbol{M}$.

3.4.4. Reassembly

With obtaining the results for interpolated shape $\bar{\boldsymbol{\Lambda}}$ and orientation $\bar{\boldsymbol{R}}$ the full interpolated tensor is reassembled following Eqn. (9) and finally yielding:

$$\bar{\boldsymbol{A}}_{\mathrm{LI}} = \bar{\boldsymbol{R}}\bar{\boldsymbol{\Lambda}}\bar{\boldsymbol{R}}^{\top}. \tag{17}$$

3.5. Comparison of the Interpolation Techniques

From a computational perspective, the Euclidean approach is superior and will always outperform its alternatives in terms of speed, since only simple additions occur and the procedure can be parallelized without any limitations. However, there are cases in which the Euclidean method can yield undesirable effects.

The linear interpolation of the components can result in tensor characterisitcs that are not interpolated monotonously. This can be illustrated by means of an simple example with only two basis values, that are chosen to

$\boldsymbol{A}_1 = \mathrm{diag}\left(< 1, 0.8, .4 >^\top\right)$ and $\boldsymbol{A}_2 = \mathrm{diag}\left(< 1, 2, 3 >^\top\right)$. Figure 4 shows the result of the interpolated K invariants using the three techniques Euclidean (EU), Log-Euclidean (Log) and Linear Invariant (LI).

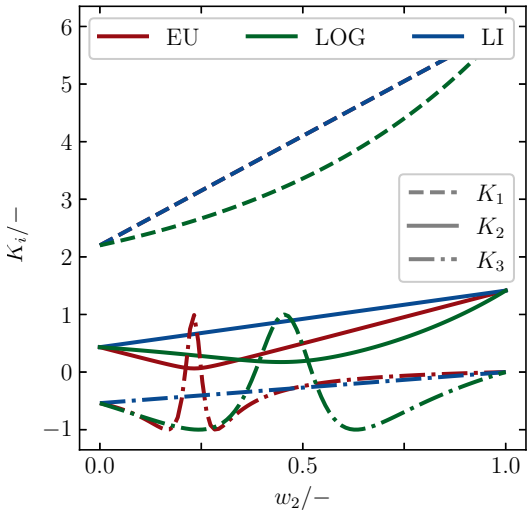

Figure 4: Course of the K invariants during one-dimensional interpolation for different interpolation schemes.

$K_1 = \mathrm{tr}\,(\boldsymbol{A})$ is interpolated monotonically for each considered method. While EU and LI methods reveal a linear connection, the LOG approach yields a non-linear behavior that is still monotonous. For the K_2 and K_3 invariants however, completely different characteristics arise: Both LOG and EU method show courses that are highly non-linear. In each case local extrema are induced due to interpolation. If the invariants possess physical significance, the effect of the values not being bounded, can become critical. In the worst case scenarios, highly over- or underestimated values may result from numerical calculation.

Another academic case is carried out to further illustrate the differences of the considered interpolation-techniques. The tensor $\boldsymbol{A}_1 = \mathrm{diag}\left(< 0.2, 0.4, 0.8 >^\top\right)$ is given. A second basis $\boldsymbol{A}_2$ is constructed by a rigid rotation of $\boldsymbol{A}_1$ by 85 deg. $\boldsymbol{A}_3$ is initialized $\boldsymbol{A}_3 = \mathrm{diag}\left(< 0.15, 0.2, 0.7 >^\top\right)$ and rotated by 75 degrees in

order to construct $\boldsymbol{A}_4$. Bi-linear interpolation is used with the EU, LOG and LI schemes. The latter is conducted with both quaternion based an dyadic orientation interpolation. Tensor glyphs in Figure 5 serve for better presentation of the results.

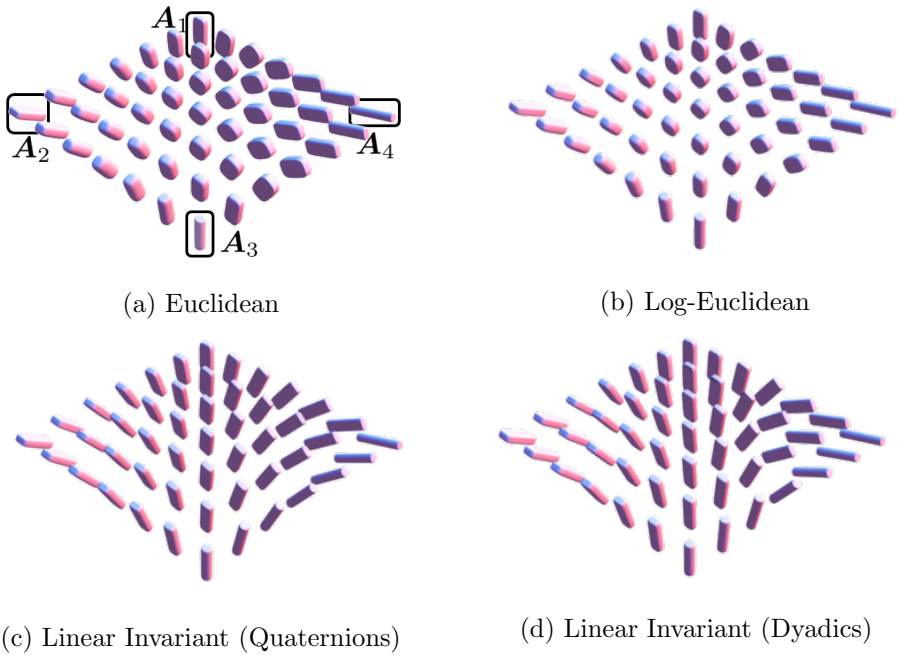

(a) Euclidean

(b) Log-Euclidean

(c) Linear Invariant (Quaternions)

(d) Linear Invariant (Dyadics)

Figure 5: Tensor glyphs for the interpolation with four different techniques. Basis values are located at the corners of the computation domain and bi-linear weight determination is used in-between. Basis values are only displayed in (a) in order to prevent redundancy.

It can be stated that the rigid rotations between $\boldsymbol{A}_1$ and $\boldsymbol{A}_2$ as well as from $\boldsymbol{A}_3$ to $\boldsymbol{A}_4$ are only captured by the Linear Invariant approaches (c), (d). Both, EU (a) and LOG (b) method, reconstruct the transition by altering tensor shape. This is achieved by preserving tensor trace or determinant, respectively. Further, the interpolation of those rotations is reproduced in a more uniform manner when using quaternions in favor of dyadics. This is related to the choice of the appropriate metric in the former case. In the following numerical investigations, the quaternion-based approach is preferred and abbreviated by LI. Generally, the variance of occurring tensor shape is larger when the EU

method is used.

4. Analytical Example

In this section the introduced interpolation approaches are extended and applied to a simple, yet application-relevant example. By deriving a continuous exact solution, a quantifiable comparison of the regarded numerical schemes is carried out.

4.1. Problem Statement

In most macroscopic process simulations of discontinuous fiber-reinforced polymers, single fibers are usually not explicitly modeled due to high computational effort. Rather statistical approaches are applied, that represent multiple fibers at a specific solution location by means of a scalar fiber orientation density function (FODF) $\psi(\boldsymbol{n})$, where $\boldsymbol{n}$ is the directional unit vector. Onat and Leckie [50] stated, that the probability density ψ can be reconstructed using its statistical higher order moments. Therefore, Advani and Tucker [51] introduced the so called fiber orientation tensor (FOT) $\boldsymbol{A}$, which is defined for a continuous FODF via

$$\boldsymbol{A} = \int_{S^2} \psi(\boldsymbol{n})\, \boldsymbol{n} \otimes \boldsymbol{n}\, \mathrm{d}S. \tag{18}$$

Herein, S^2 is the 2-Sphere. In the case of a finite number $N \in \mathbb{N}$ of discrete fibers, Eqn. (18) reduces to $\boldsymbol{A} = \frac{1}{N}\sum_I^N \boldsymbol{n}_I \otimes \boldsymbol{n}_I$. From this definition, the symmetric and positive semidefinite properties of $\boldsymbol{A}$ are evident [52].

In various composite processes, liquid polymer is infiltrated or infused into the mold by means of a plane point sprue. In proximity to the point sprue, the analytical expression for the velocity field is derived from the conservation of volume: $\boldsymbol{v} = r_0/r\, v_0 \boldsymbol{e}_r$ with v_0 being the velocity at inner radius r_0 of the point sprue. Thus, the spin-free spatial velocity gradient follows as $\boldsymbol{L} = \boldsymbol{D} = -\frac{v_0 r_0}{r^2}(\boldsymbol{e}_r \otimes \boldsymbol{e}_r - \boldsymbol{e}_\varphi \otimes \boldsymbol{e}_\varphi)$. Following the transport equation as introduced in [51], a stationary solution of the fiber orientation tensor distribution is described by the boundary value problem:

$$\frac{\partial \boldsymbol{A}}{\partial \boldsymbol{x}}\boldsymbol{v} = 2\lambda\left(\mathrm{sym}\left(\boldsymbol{A}\boldsymbol{D}\right) - \left(\boldsymbol{A}\otimes\boldsymbol{A}\right)\boldsymbol{D}\right) \qquad ;\forall \boldsymbol{x}\in\{\boldsymbol{x}\cdot\boldsymbol{x} > r_o^2\} \tag{19}$$

$$\boldsymbol{A} = \boldsymbol{A}_0 \in \{\mathrm{PSYM} \cap \boldsymbol{A}_0\cdot\boldsymbol{I} = 1\} \qquad ;\forall \boldsymbol{x}\in\{\boldsymbol{x}\cdot\boldsymbol{x} = r_o^2\} \tag{20}$$

Herein, λ is a scalar factor, depending on the fibers' aspect ratio. By choosing the quadratic closure approach $\mathbb{A} = \boldsymbol{A}\otimes\boldsymbol{A}$ as introduced in [51] and a diagonal boundary value $\boldsymbol{A}_0 = A_{r,0}\boldsymbol{e}_r\otimes\boldsymbol{e}_r + A_{\varphi,0}\boldsymbol{e}_\varphi\otimes\boldsymbol{e}_\varphi + A_{z,0}\boldsymbol{e}_z\otimes\boldsymbol{e}_z$, the set of first-order ODEs in Eqn. (19) is decoupled within the cylindrical coordinate system and yields a closed form explicit expression for the components of $\boldsymbol{A}$ for all r satisfying $r \geq r_0$:

$$A_{rr} = \frac{A_{r,0}\, r_0^{4\lambda}\, r^{-2\lambda}}{A_{r,0}\, r_0^{4\lambda}\, r^{-2\lambda} + A_{\varphi,0}\, r^{2\lambda} + A_{z,0}\, r_0^{2\lambda}} \tag{21}$$

$$A_{\varphi\varphi} = \frac{A_{\varphi,0}\, r^{4\lambda}}{A_{r,0}\, r_0^{4\lambda}\, r^{-2\lambda} + A_{\varphi,0}\, r^{2\lambda} + A_{z,0}\, r_0^{2\lambda}} \tag{22}$$

$$A_{zz} = 1 - A_{rr} - A_{\varphi\varphi}, \tag{23}$$

$$A_{r\varphi} = A_{rz} = A_{\varphi z} = 0. \tag{24}$$

It may be noted, that research has proposed various additional right-hand side terms to Eqn. (19) accounting for diffusion or advection as a consequence of fiber interaction[53, 54, 55, 56], which are deliberately neglected in this context in order to obtain an analytical expression to the stated BVP. Further, the solution does not depend on the value of the inlet velocity, since all transport mechanisms are linear in v_0 and thus cancel each other out. By normalizing all occurring distances through inlet radius r_0, the problem becomes nondimensionalized. As Figure 6 reveals, radial terms A_{rr} and out-of plane terms A_{zz} vanish in favor of tangential alignment with $A_{\varphi\varphi}$ converging towards 1 with increasing distance to the origin.

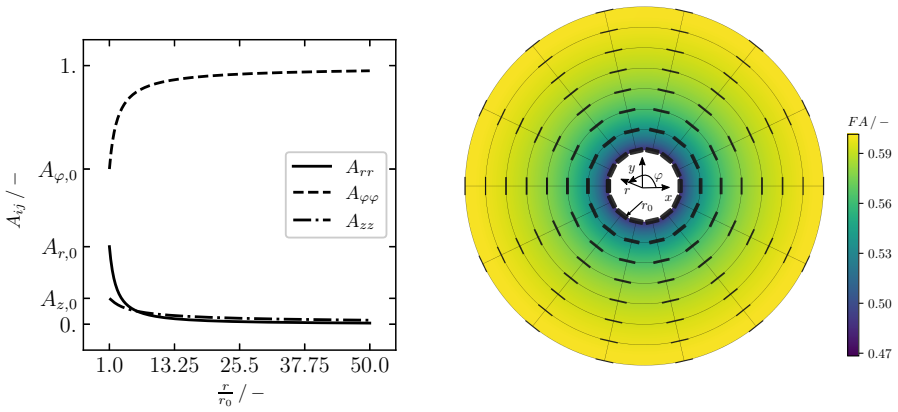

Figure 6: Solution for the BVP from Equation (19) with parameter set $\{A_{r,0} = 0.3, A_{\varphi,0} = 0.6, A_{zz} = 0.1, \lambda = 0.3\}$. Left-hand side: Course of the components of the fiber orientation tensor $\boldsymbol{A}$ as a function of the normalized distance r/r_0. Right-hand side: Tensor glyphs of the solution reveal the tendency to uni-axial orientation states in the far field of the point sprue over the contour plot of the fractional anisotropy FA

4.2. Numerical Study

In the next step, the analytical solution given in Equation (21) shall be used to compare the addressed interpolation techniques. For the purpose of interpolation, it is assumed that the solution has been obtained by a numerical solver or has been measured in an experimental setup and therefore is only accessible at discrete points. In order to emulate a typical data transfer procedure from process simulation to structural simulation, the fiber orientation tensors are mapped onto a virtual non-congruent discretization. Literature gives several studies in which this step has been conducted in order to estimate effective (thermo-) mechanical composite properties by means of mean-field homogenization [4, 57, 58, 59, 60, 61].

4.2.1. Procedure and Error Metrics

Error measurement for tensor fields is not straight-forward, since it requires reduction to a single scalar value. In this work, three singular local errors between exact $(\cdot)$ and approximated $\bar{(\cdot)}$ value are to be considered: The Frobenius

norm $\sqrt{\boldsymbol{A} \cdot \boldsymbol{A}} = \|\boldsymbol{A}\|$ corresponds to the Euclidean metric and therefore is the natural choice for the Euclidean interpolation scheme (EU), while the determinant is directly connected to Log-Euclidean (LOG). The fractional anisotropy $FA = R_2$ is chosen to assess the interpolated tensor shape.

The procedure to determine the local errors ϵ at a specific location $(x, y)^\top$ is implemented as depicted in figure 7:

Algorithm 2 Determination of the approximation errors

1: **procedure** LOCAL ERROR(x, y, δ)
2: $\quad \boldsymbol{A} \leftarrow \boldsymbol{A}_{\text{ana}}\left(\sqrt{x^2 + y^2}\right)$
3: $\quad r_I \leftarrow \sqrt{(x \pm \delta/2)^2 + (y \pm \delta/2)^2}$
4: $\quad \boldsymbol{A}_I \leftarrow \boldsymbol{A}_{\text{ana}}(r_I)$
5: $\quad \bar{\boldsymbol{A}} \leftarrow \bar{\boldsymbol{\phi}}(\boldsymbol{A}_I, w_I)$
6: $\quad$ **return** $\epsilon\left(\bar{\boldsymbol{A}}, \boldsymbol{A}\right)$

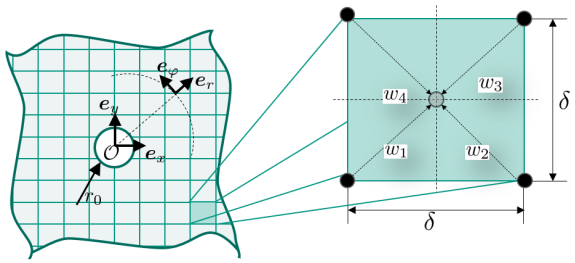

Figure 7: Problem statement for the analytical example discretization. A virtual rectangular computation grid is superimposed on the continuous space. FOTs are interpolated at locations within the cell (gray) using the nodes (black) as basis values.

Herein, δ represents the grid size of the rectangular virtual source mesh cell. Weights w_I are determined via a bi-linear shape-function approach.

4.2.2. Results and Discussion

Evaluation is conducted for locations along the line $y = 1/3\,x$. The influence of mesh fineness is considered by conducting the numerical study with varying

normalized grid sizes δ/r_0. Figure 8 shows the results of the numerical study for the error metrics introduced in Section 4.2.1.

Two universal trends are identifiable for each combination of error metric and selected interpolation technique: First, the local relative errors are vanishing with increasing distance from the inlet at $r = r_0$. Second, the displayed errors correlate negatively with grid lengths δ. Both observations can be explained by the occurring gradients, that vanish with increasing r, since the state converges (cf. Figure 6). Higher values for δ are accompanied by major differences between the basis values used for interpolation.

With focus on the Frobenius error depicted in Figure 8 (a), results reveal significantly better performance in the case of the LI method compared to EU and LOG even for coarse discretization. The same behavior can also be seen when considering FA and determinant as illustrated in Figure 8 (b) and (c), respectively. It is worth mentioning that in the latter case, both EU and LI method have the tendency of predicting values that are too low. The LOG technique on the other hand underestimates the determinant in this analytical example.

This rather simple example problem shows that the choice of interpolation technique actually has an influence on the results obtained. In this case, the relative errors are just in the single-digit percent range. However, if higher gradient or even jumps and singularities arise in more complex problems, the observed effects are likely to be intensified.

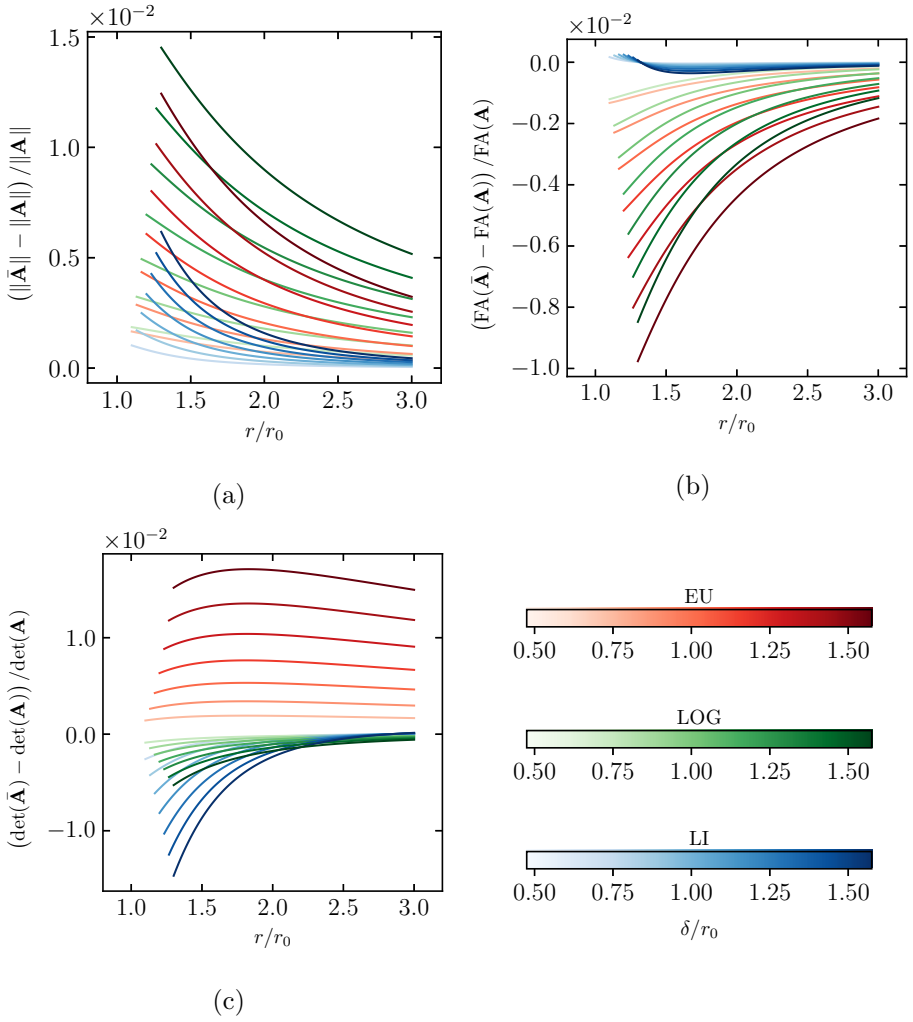

Figure 8: Local interpolation errors of the three interpolation schemes (EU, LOG, LI) for the point sprue problem as a function of normalized distance to inlet r/r_0 and characteristic grid length δ/r_0

5. Numerical Example: Field Recovery

From the observations conducted on the analytical example and outlined in the previous chapter, the influence of the choice of the applied interpolation scheme has to be investigated on a higher scale, emulating the CAE workflow

in a connected virtual manufacturing chain. For this purpose an actual injection molding case is set up and solved via the numerical computational fluid dynamics (CFD) solver Moldflow 2018.

5.1. Problem Statement

The problem at hand is a generic plate with dimensions 200 mm × 200 mm × 10 mm, that is filled with discontinuous fiber-reinforced thermoplastic via an inlet located at the lower left corner at an constant, predefined volume flow. FOTs are computed at each cell center. Figure 9 illustrates the dimensions as well as the approximated solution of the CFD simulation in terms of FOTs. The represented tensor-valued field shows strong inhomogeneities across the solution domain. In the near field of the inlet a trend towards anisotropy with principle directions perpendicular to local velocity vectors can be observed. Isotropic distributions are more frequent and pronounced in proximity of the corners distant to the inlet.

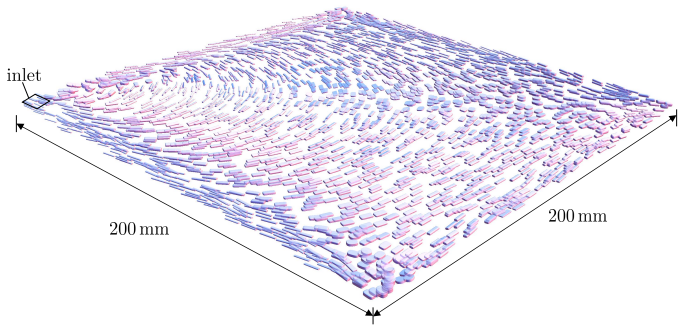

Figure 9: Problem dimensions and results of the CFD simulation for fiber orientation tensors.

5.2. Numerical Study

It is assumed that the computed discrete data is mapped onto a non-congruent structural mesh, where the FOTs are used to determine magnitude and orientation of local stiffnesses and coefficients of thermal expansion.

5.2.1. Recovery Procedure and Statistical Evaluation

In order to be able to give statements about the mapping quality, an approach of field recovery via interpolation is conducted: N_d computed values at specific locations in the solution domain are artificially deleted and reconstructed by means of the N_r remaining values. The value obtained as a result is then compared on the different metrics introduced in section 4. Weights are determined using the inverse distance method as introduced by Shepard [12] choosing the power parameter $p = 2$.

$$w_I(\boldsymbol{x}) = \frac{1}{\|\boldsymbol{x}_I - \boldsymbol{x}\|^p} \frac{1}{\sum_J \|\boldsymbol{x}_J - \boldsymbol{x}\|^{-p}} \quad \forall\, \boldsymbol{x}_J : \|\boldsymbol{x}_J - \boldsymbol{x}\| \leq d_0 \tag{25}$$

Search distance d_0 is set dynamically, guaranteeing four basic values to be located within the sphere of influence for each case. The choice of the deleted values is defined by random sampling neglecting specific location and cell neighborhood. In order to reduce the influence of this selection, a total of 35 numerical experiments with varying random sampling is conducted. Statistical analysis is carried out across the entirety of these experiments. The median Q_2 is defined as statistical measure of determination.

The complete procedure consisting of value erasure, field recovery and statistical evaluation is performed for varying information density $\rho = N_\mathrm{r}/(N_\mathrm{r} + N_\mathrm{d})$. This is supposed to emulate differently pronounced mismatches between characteristic mesh lengths from source to target discretization.

5.2.2. Results and Discussion

The results of the numerical study are plotted for visual interpretation in Figure 10. In each plot displayed, the error medians of the experiments are represented through solid circle markers. Continuous lines are graphs of nonlinear analytical fittings obtained by regression. For the Frobenius norm of the local relative interpolation error – depicted in sub-plot (a) – a strong trend is emerging: For each of the three investigated interpolation schemes, the error median grows in a degressive manner with increasing inverse information density ρ^{-1}. The good accordances with the quadratic model of the type $Q_2^2 \propto \rho^{-1}$

confirm this observation. With minor differences for smaller values of ρ^{-1}, the LI approach starts to outperform both LOG and EU method, when the number of basic values is decreasing.

The statement also holds for the median error on the fractional anisotropy measure FA in Fig. 10 (b). A systematic underestimation is demonstrated with this example in any case. As in the aforementioned case, errors do also evolve following a quadratic tendency. It is noteworthy, that the median error resulting from the application of the LI method is considerably lower compared to both other approaches. However, these findings do not necessarily indicate that the LI-method yields lower local errors in each case, since positive and negative values may cancel each other out. Still, it implies little systematic bias is introduced by the LI method on this metric.

In the case of the determinant error metric in Fig. 10 (c), the evolution of the median local errors reveal an systematic overestimation in the case of the EU approach, even for high information density, while the LI and LOG methods produce too low values on average. From an absolute perspective, the LOG interpolation scheme generates the lowest statistical bias, which is expected, since the interpolation schemes were originally introduced in order to guarantee monotony of this measure. In this case, the error evolutions are approximated with a cubic model of the type $Q_2^3 \propto \rho^{-1}$.

As an additional error metric, the angular deviation of the first Eigenvector $\boldsymbol{p}_1$ has been investigated. The graphs of the error courses (d) reveal minor differences between the three considered interpolation schemes. It may also be noted, that the absolute values of this systematic errors are within the per mille range and therefore generally lower by an order of magnitude compared to the FA-errors and even two orders of magnitude compared to the Frobenius and determinant errors, respectively.

To conclude this numerical study, it should be kept, that significant statistical bias can be induced through interpolation, depending on both the choice of the interpolation scheme and the regarded error metric. When invariants are considered and processed in a subsequent step, the conventional EU method

may not necessarily be the best choice, especially if pronounced gradients occur and the information is transferred onto a finer discretization. In this case tensor shape is interpolated incorrectly due to overestimated isotropy. Therefore, an interpolation approach should rather be used, which is is able to interpolate the desired invariant monotonously. For the orientation interpolation, only negligible differences and very small errors could be observed.

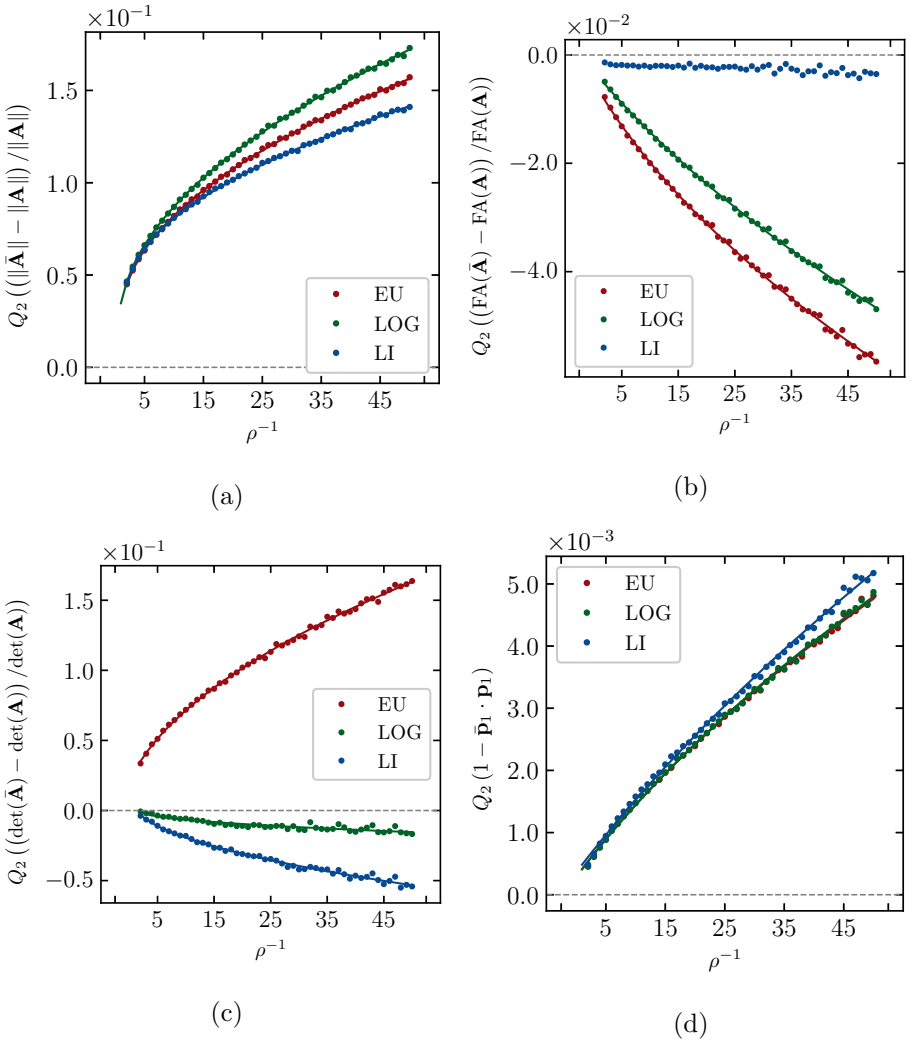

Figure 10: Medians Q_2 of the interpolation errors of the fiber orientation tensor $\boldsymbol{A}$ for the plate problem as a function of the inverse information density ρ^{-1}.

6. Conclusion and Outlook

A broad overview of existing conventional and more sophisticated tensor interpolation techniques is presented and approaches to close existing gaps in the orientation interpolation of an arbitrary numbers of input tensorial basic values are proposed and carried out. A selection from the outlined interpolation techniques is implemented and applied upon two simple purely mathematical problems. Fundamental differences and characteristics are elaborated and discussed. It becomes evident that conventional Euclidean interpolation (EU), introduces significant non-monotonic behavior in tensor shape, which can result in local extrema between basis values. The amount of artificial isotropy due to interpolation can be reduced when applying a sophisticated approach based upon decoupled interpolation of tensor shape and tensor orientation. For this purpose sets of orthogonal tensor invariants were used and interpolated in linear manner (LI method).

Eventually, focus is changed to application and use cases are chosen in the context of process simulation for injection molding of short fiber-reinforced thermoplastics.To quantitatively evaluate the considered interpolation techniques, an analytical example is constructed by means of the near field of a point sprue. The obtained continuous and deterministic solution for the field of 2^{nd}-order fiber orientation tensors is then consulted and compared to values computed by reconstruction via interpolation. Results confirm good performance of the advanced linear-invariant method (LI) on different metrics. On the next step, a CDF simulation of an injection molded generic plate is performed. Information is deleted from the solution and interpolation is used to reconstruct the omitted values. The procedure is repeated for different information densities and randomized samples. Afterwards, statistical evaluation is performed revealing trends and systematic errors. Again, an overestimating bias in tensor shape inducing artificial isotropy can be detected on this higher-level when using conventional global interpolation methods.

Although broadly applied in engineering workflows, the transfer of tensor

valued data is not as straightforward as it may appear on first sight. It is shown, which undesired effects may result when interpolating on tensor-valued fields. Hence, users should be aware of the occuring problems and the further utilization of results. Based upon these considerations, a suitable interpolation technique should be selected – or otherwise a user should preferably rely on non-interpolating mapping techniques to be on the safe side. Future work will focus on the evaluation of the actual impact on global performance and adapting invariants-based interpolation techniques towards stress tensor interpolation, where additional requirements have to be taken into account.

Acknowledgment

The authors would like to thank the German Federal Ministry of Education and Research (BMBF) for their funding of the research project *ITEA VMAP* (Gn. 01IS17025) in whose context the work at hand has been established. The work is also part of the Young Investigators Group (YIG) *Green Mobility – Tailored Composite Materials for Lightweight Structures* funded by the Vector foundation.

References

[1] J. Seuffert, L. Kärger, F. Henning, Simulating mold filling in compression resin transfer molding (crtm) using a three-dimensional finite-volume formulation, Journal of Composites Science 2 (04 2018). doi:10.3390/jcs2020023.

[2] F. Henning, L. Kärger, D. Dörr, F. J. Schirmaier, J. Seuffert, A. Bernath, Fast processing and continuous simulation of automotive structural composite components, Composites Science and Technology 171 (2019) 261 – 279. doi:https://doi.org/10.1016/j.compscitech.2018.12.007.

[3] L. Kärger, A. Bernath, F. Fritz, S. Galkin, D. Magagnato, A. Oeckerath, A. Schön, F. Henning, Development and validation of a cae chain for unidi-

rectional fibre reinforced composite components, Composite structures 132 (2015) 350–358. doi:10.1016/j.compstruct.2015.05.047.

[4] J. Görthofer, N. Meyer, T. D. Pallicity, L. Schöttl, A. Trauth, M. Schemmann, M. Hohberg, P. Pinter, P. Elsner, F. Henning, A. Hrymak, T. Seelig, K. Weidenmann, L. Kärger, T. Böhlke, Virtual process chain of sheet molding compound: Development, validation and perspectives, Composites / B 169 (2019) 133–147. doi:10.1016/j.compositesb.2019.04.001.

[5] J. Görthofer, N. Meyer, T. D. Pallicity, L. Schöttl, A. Trauth, M. Schemmann, M. Hohberg, P. Pinter, P. Elsner, F. Henning, A. Hrymak, T. Seelig, K. Weidenmann, L. Kärger, T. Böhlke, Motivating the development of a virtual process chain for sheet molding compound composites, PAMM 19 (11 2019). doi:10.1002/pamm.201900124.

[6] N. Mayer, J. Prowe, T. Havar, R. Hinterhoelzl, K. Drechsler, Structural analysis of composite components considering manufacturing effect, Composite Structures 140 (2016) 776–782. doi:10.1016/j.compstruct.2016.01.023.

[7] N. Mayer, B. Broucke, J. Prowe, T. Havar, R. Hinterhoelzl, Finite element mapping for incompatible fe meshes of composite structures, Advances in Engineering Software 99 (2016) 81–88. doi:10.1016/j.advengsoft.2016.05.007.

[8] P. Breiding, K. Kozhasov, A. Lerario, On the geometry of the set of symmetric matrices with repeated eigenvalues, Arnold Mathematical Journal (01 2019). doi:10.1007/s40598-018-0095-0.

[9] G. Kindlmann, Superquadric tensor glyphs, 2004, pp. 147–154. doi:10.2312/VisSym/VisSym04/147-154.

[10] T. Schultz, G. Kindlmann, Superquadric glyphs for symmetric second-order tensors, IEEE transactions on visualization and computer graphics 16 (2011) 1595–604. doi:10.1109/TVCG.2010.199.

[11] M. Barczy, P. Burai, Limit theorems for bajraktarević and cauchy quotient means of independent identically distributed random variables, Aequationes mathematicae 96 (04 2022). doi:10.1007/s00010-021-00813-x.

[12] D. Shepard, A two-dimensional interpolation function for irregularly-spaced data, ACM National Conference 23 (1968) 517–524. doi:10.1145/800186.810616.

[13] M. Buhmann, Radial basis functions, Acta Numerica 2000 9 (01 2000). doi:10.1017/S0962492900000015.

[14] A. Tolstykh, D. Shirobokov, On using radial basis functions in a "finite difference mode" with applications to elasticity problems, Computational Mechanics 33 (2003) 68–79. doi:10.1007/s00466-003-0501-9.

[15] Antônio Francisco Neto, An approach to isotropic tensor functions and their derivatives via omega matrix calculus, Journal of Elasticity 141 (2020) 165–180.

[16] F. Nielsen, R. Bhatia, Matrix Information Geometry, 2013.

[17] E. Meijering, A chronology of interpolation: From ancient astronomy to modern signal and image processing, Proceedings of the IEEE 90 (2002) 319 – 342. doi:10.1109/5.993400.

[18] P. Batchelor, M. Moakher, D. Atkinson, F. Calamante, A. Connelly, A rigorous framework for diffusion tensor calculus, Magnetic resonance in medicine : official journal of the Society of Magnetic Resonance in Medicine / Society of Magnetic Resonance in Medicine 53 (2005) 221–5. doi:10.1002/mrm.20334.

[19] P. Fletcher, S. Joshi, Principal geodesic analysis on symmetric spaces: Statistics of diffusion tensors, Vol. 3117, 2004, pp. 87–98. doi:10.1007/978-3-540-27816-0_8.

[20] M. Moakher, A differential geometric approach to the geometric mean of symmetric positive-definite matrices, SIAM J. Matrix Analysis Applications 26 (2005) 735–747. doi:10.1137/S0895479803436937.

[21] F. Hiai, D. Petz, Riemannian metrics on positive definite matrices related to means. ii, Linear Algebra and its Applications 436 (7) (2012) 2117 – 2136. doi:https://doi.org/10.1016/j.laa.2011.10.029.

[22] F. Yang, Y.-M. Zhu, I. E. Magnin, J.-H. Luo, P. Croisille, P. B. Kingsley, Feature-based interpolation of diffusion tensor fields and application to human cardiac dt-mri, Medical image analysis 16 (2) (2012) 459–481.

[23] V. Arsigny, P. Fillard, X. Pennec, N. Ayache, Log-euclidean metrics for fast and simple calculus on diffusion tensors, Magnetic resonance in medicine : official journal of the Society of Magnetic Resonance in Medicine / Society of Magnetic Resonance in Medicine 56 (2006) 411–21. doi:10.1002/mrm.20965.

[24] V. Arsigny, P. Fillard, X. Pennec, N. Ayache, Fast and simple computations on tensors with log-euclidean metrics., INRIA Res Rep (01 2005).

[25] I. Hameduddin, T. A. Zaki, the mean conformation tensor in viscoelastic turbulence, Journal of Fluid Mechanics 865 (2019) 363–380. doi:10.1017/jfm.2019.46.

[26] Ke Gao, J. P. Harrison, Mean and dispersion of stress tensors using euclidean and riemannian approaches, International Journal of Rock Mechanics and Mining Sciences 85 (2016) 165–173. doi:https://doi.org/10.1016/j.ijrmms.2016.03.019.

[27] Xin Huang, M. Xu, Z. Zhang, Q. Lei, Characterizing stress variability within granular samples upon liquefaction, Computers and Geotechnics 127 (2020) 103771. doi:https://doi.org/10.1016/j.compgeo.2020.103771.

[28] G. Brèthes, A. Dervieux, A tensorial-based mesh adaptation for a poisson problem, European Journal of Computational Mechanics 26 (3) (2017) 245–281. doi:10.1080/17797179.2017.1310648.

[29] Modesar Shakoor, C. H. Park, A higher order finite element method with unstructured anisotropic mesh adaption for two phase flows with surface tension, Computers and Fluids 230 (2021) 105154. doi:https://doi.org/10.1016/j.compfluid.2021.105154.

[30] W. J. Culver, On the existence and uniqueness of the real logarithm of a matrix, Proceedings of the American Mathematical Society 17 (5) (1966) 1146–1151.

[31] X. Pennec, P. Fillard, N. Ayache, P. Epidaure, A riemannian framework for tensor computing, International Journal of Computer Vision 66 (08 2004). doi:10.1007/s11263-005-3222-z.

[32] K. M. Hasan, P. J. Basser, D. L. Parker, A. L. Alexander, Analytical computation of the eigenvalues and eigenvectors in dt-mri, Journal of Magnetic Resonance 152 (1) (2001) 41–47.

[33] P. Basser, S. Pajevic, Statistical artefacts in diffusion tensor mri (dt-mri) caused by background noise, Magnetic resonance in medicine : official journal of the Society of Magnetic Resonance in Medicine / Society of Magnetic Resonance in Medicine 44 (2000) 41–50.

[34] S. Jung, A. Schwartzman, D. Groisser, Scaling-rotation distance and interpolation of symmetric positive-definite matrices, SIAM Journal on Matrix Analysis and Applications 36 (3) (2015) 1180–1201. doi:10.1137/140967040.

[35] L. Zhukov, A. Barr, Oriented tensor reconstruction: tracing neural pathways from diffusion tensor mri, in: IEEE Visualization, 2002. VIS 2002., 2002, pp. 387–394. doi:10.1109/VISUAL.2002.1183799.

[36] D. Ennis, G. Kindlmann, Orthogonal tensor invariants and the analysis of diffusion tensor magnetic resonance images, Magnetic resonance in medicine : official journal of the Society of Magnetic Resonance in Medicine / Society of Magnetic Resonance in Medicine 55 (2006) 136–46. doi:10.1002/mrm.20741.

[37] J. K. Gahm, G. Kindlmann, D. Ennis, The effects of noise over the complete space of diffusion tensor shape, Medical image analysis 18 (2013) 197–210. doi:10.1016/j.media.2013.10.009.

[38] J. K. Gahm, N. Wisniewski, G. Kindlmann, G. Kung, W. Klug, A. Garfinkel, D. Ennis, Linear invariant tensor interpolation applied to cardiac diffusion tensor mri, Vol. 15, 2012, pp. 494–501. doi:10.1007/978-3-642-33418-4_61.

[39] G. Kindlmann, R. Estépar, M. Niethammer, S. Haker, C.-F. Westin, Geodesic-loxodromes for diffusion tensor interpolation and difference measurement, Vol. 10, 2007, pp. 1–9. doi:10.1007/978-3-540-75757-3_1.

[40] Z. Lan, B. Reich, J. Guinness, D. Bandyopadhyay, L. Ma, F. Moeller, Geostatistical modeling of positive definite matrices: An application to diffusion tensor imaging, Biometrics (02 2021). doi:10.1111/biom.13445.

[41] E. Teich, M. Cieslak, B. Giesbrecht, J. Vettel, S. Grafton, T. Satterthwaite, D. Bassett, Crystallinity characterization of white matter in the human brain, New Journal of Physics 23 (07 2021). doi:10.1088/1367-2630/ac1286.

[42] C. Gramkow, On averaging rotations, Journal of Mathematical Imaging and Vision 15 (1) (2001) 7–16.

[43] M. Moakher, Means and averaging in the group of rotations, SIAM Journal on Matrix Analysis and Applications 24 (04 2002). doi:10.1137/S0895479801383877.

[44] J. Lawson, Y. Lim, Karcher means and karcher equations of positive definite operators, Transactions of the American Mathematical Society, Series B 1 (1) (2014) 1–22.

[45] S. Han, O. A. Bauchau, On the global interpolation of motion, Computer Methods in Applied Mechanics and Engineering 337 (2018) 352 – 386. doi:https://doi.org/10.1016/j.cma.2018.04.002.

[46] J. K. Gahm, D. Ennis, Dyadic tensor-based interpolation of tensor orientation: Application to cardiac dt-mri, 2013, pp. 135–142. doi:10.1007/978-3-642-54268-8_16.

[47] F. L. Markley, Y. Cheng, Averaging quaternions, Journal of Guidance, Control, and Dynamics 30 (4) (2007) 1193–1197. doi:10.2514/1.289490.

[48] M.-J. Kim, M.-S. Kim, S. Y. Shin, A compact differential formula for the first derivative of a unit quaternion curve, The Journal of Visualization and Computer Animation 7 (1) (1996) 43–57.

[49] S. Bonnabel, R. Sepulchre, Riemannian metric and geometric mean for positive semidefinite matrices of fixed rank, SIAM Journal on Matrix Analysis and Applications 31 (3) (2010) 1055–1070. doi:10.1137/080731347.

[50] E. T. Onat, F. A. Leckie, Representation of Mechanical Behavior in the Presence of Changing Internal Structure, Journal of Applied Mechanics 55 (1) (1988) 1–10. doi:10.1115/1.3173630.

[51] S. Advani, C. Tucker, The use of tensors to describe and predict fiber orientation in short fiber composites, Journal of Rheology 31 (8) (1987) 751–784. doi:10.1122/1.549945.

[52] Julian Karl Bauer, T. Böhlke, Variety of fiber orientation tensors, Mathematics and Mechanics of Solids 0 (0) (2021) 10812865211057602.

[53] F. Folgar, I. Charles L. Tucker, Orientation behavior of fibers in concentrated suspensions, Journal of Reinforced Plastics and Composites 3 (2) (1984) 98–119. doi:10.1177/073168448400300201.

[54] J. Wang, J. O'Gara, C. Tucker, An objective model for slow orientation kinetics in concentrated fiber suspensions: Theory and rheological evidence, Journal of Rheology - J RHEOL 52 (09 2008). doi:10.1122/1.2946437.

[55] J. Phelps, C. Tucker, An anisotropic rotary diffusion model for fiber orientation in short- and long-fiber thermoplastics, Journal of Non-Newtonian Fluid Mechanics 156 (3) (2009) 165–176. doi:10.1016/j.jnnfm.2008.08.002.

[56] S. K. Kugler, G. M. Lambert, C. Cruz, A. Kech, T. A. Osswald, D. G. Baird, Macroscopic fiber orientation model evaluation for concentrated short fiber reinforced polymers in comparison to experimental data, Polymer Composites 41 (7) (2020) 2542–2556. doi:10.1002/pc.25553.

[57] W. Ogierman, G. Kokot, a study on fiber orientation influence on the mechanical response of a short fiber composite structure, Acta Mechanica 227 (2016) 173–183.

[58] F. Buck, B. Brylka, V. Müller, T. Mueller, K. Weidenmann, A. Hrymak, F. Henning, T. Böhlke, Two-scale structural mechanical modeling of long fiber reinforced thermoplastics, Composites Science and Technology 117 (06 2015). doi:10.1016/j.compscitech.2015.05.020.

[59] A. Trauth, L. Kehrer, P. Pinter, K. Weidenmann, T. Böhlke, On the effective elastic properties based on mean-field homogenization of sheet molding compound composites, Composites Part C: Open Access 4 (2020) 100089. doi:10.1016/j.jcomc.2020.100089.

[60] V. Romanenko, M. Duhovic, D. Schommer, J. Hausmann, J. Eschl, Advanced process simulation of compression molded carbon fiber sheet molding compound (c-smc) parts in automotive series applications, Composites Part A: Applied Science and Manufacturing 157 (2022) 106924. doi:10.1016/j.compositesa.2022.106924.

[61] T. Russell, B. Heller, D. Jack, D. Smith, Prediction of the fiber orientation state and the resulting structural and thermal properties of fiber reinforced additive manufactured composites fabricated using the big area additive manufacturing process, Journal of Composites Science 2 (2018) 26. doi:10.3390/jcs2020026.